

EXPERIMENTAL ANALYSIS OF A HIGH-SPEED-RAILWAY EMBANKMENT INTERSECTING STEEP GROUND FISSURES AT DIFFERENT ANGLES

EKSPERIMENTALNA ANALIZA ŽELEZNIŠKEGA NASIPA HITRE ŽELEZNICE, KI SEKA POD RAZLIČNIMI KOTI STRME RAZPOKE V TLEH

Jianbing Peng (*corresponding author*)
Chang'an University,
Key Laboratory of Western China's Mineral Resources and Geological Engineering of Ministry of Education
Xi'an 710054, China
E-mail: dicexy_01@126.com

Zhongjie Fan (*corresponding author*)
Changjiang River Scientific Research Institute of Changjiang Water Resources Commission, Wuhan 430010, China; and Chengdu University of Technology, State Key Laboratory of Geohazard Prevention and Geoenvironment Protection, Chengdu 610059, China
E-mail: stephenf88@163.com

Cong Liu
Chang'an University,
College of the Geology Eng. and Geomatics, Department of Geology Engineering
Xi'an 710054, China
E-mail: liucong@chd.edu.cn

Qiangbing Huang
Chang'an University,
College of the Geology Eng. and Geomatics, Department of Geology Engineering
Xi'an 710054, China
E-mail: dcdgx24@chd.edu.cn

Jigen Liu
Changjiang River Scientific Research Institute of Changjiang Water Resources Commission; and Research Center on Mountain Torrent and Geologic Disaster Prevention of Ministry of Water Resources
Wuhan 430010, China
E-mail: jigenliu@163.com

Hongyu Ren
Changjiang River Scientific Research Institute of Changjiang Water Resources Commission; and Research Center on Mountain Torrent and Geologic Disaster Prevention of Ministry of Water Resources
Wuhan 430010, China
E-mail: hongyuren@126.com

Ming Wu
Chang'an University,
College of the Geology Eng. and Geomatics, Department of Geology Engineering
Xi'an 710054, China
E-mail: eagleming@chd.edu.cn

Zhenjiang Meng
Chang'an University,
College of the Geology Eng. and Geomatics, Department of Geology Engineering
Xi'an 710054, China
E-mail: mengzj@chd.edu.cn

DOI <https://doi.org/10.18690/actageotechslov.16.1.13-29.2019>

Keywords

ground fissure; high-speed-railway embankment; orthogonal intersection; physical simulation experiments

Ključne besede

razpoka v tleh; nasip hitrih železnic; pravokotno sekanje; fizikalni simulacijski eksperiment

Abstract

A high-speed-railway (HSR) embankment intersection with ground fissures is a commonly encountered engineering problem. This paper reports a series of experiments conducted on a reduced scale to investigate the influence of different ground-fissure intersection angles on a HSR embankment. The tests revealed the presence of an integrated bend-tension failure mode in the embankment's reinforced concrete (RC) slab as a result of activities asso-

Izvleček

Križanja nasipov hitrih železnic (nasip HŽ) z zemeljskimi razpokami predstavljajo pogost inženirski problem. V prispevku je predstavljen niz eksperimentov, izvedenih v zmanjšanem merilu, s katerimi je raziskan vpliv različnih kotov križanja razpok v tleh z nasipom HŽ. Preizkusi so pokazali prisotnost integriranega načina upogibne natezne porušitve v armiranem betonu (AB) nasipa, kot posledico aktivnosti, povezanih z razpokami v tleh. Rezultati so

ciated with ground fissures. The results showed that the length and the area of the RC slab failure zone decreased nonlinearly with an increasing intersection angle, while the pile load and pile end-bearing varied to different extents in the foundations as they were affected by the slab deformation and rotation. Although the smallest effect on the embankment was observed when the ground fissure intersected the HSR orthogonally, traditional designs that incorporated this do not meet the minimum safety standards. The results of this study show that train-load-induced embankment settlement is insignificant compared with that induced by ground fissures. Therefore, this effect should be given priority in the design of alternative HSR embankments, especially for those in fissure-prone areas.

1 INTRODUCTION

Ground fissures are widespread geohazards that manifest as discontinuous, broken planes in the surface of the Earth [20, 28]. These fissures are generally divided into two categories, depending on their formation under the control of tectonics (i.e., tectonically or non-tectonically controlled) [26]. Of these, the latter is most often the result of human activity, dilative soil, soil collapse, and drought [9, 15, 18, 22]. Ground fissures caused by groundwater pumping are very common in areas where there is a shortage of water, including the southwestern American basin, the north China plain, and in northeastern Africa [29]. Tectonically controlled fissures usually develop in areas of intense structural activity and are dictated by the regional stress field, thereby exhibiting a stable strike orientation that is generally parallel to the substratum structural lines [6, 12, 14, 23]. Some tectonic ground fissures can also be strongly affected by groundwater pumping, thereby posing serious dangers to nearby buildings and residents [2, 8, 13]. To address these severe hazards, a number of studies have been conducted relating to the influence of ground fissures on buildings and underground constructions. The failure mechanisms associated with ground fissures have also been investigated in detail [20, 21, 27].

As construction has developed, additional engineering challenges have come to light, including the significant threat posed to HSRs by ground fissures [10]. Train-load and ground fissures are both vital factors that lead to the post-construction settlement of HSRs in areas of intense tectonic activity [5]. Of these, the former has been studied thoroughly, using a range of different approaches [1, 24, 25]. Various engineering methods, including geogrid-reinforced pile-raft-supported (GRPS) embankments and bridges, have been used to control the

pokazali, da se dolžina in površina porušne cone AB plošče nelinearno zmanjšujeta z naraščajočim kotom križanja, medtem ko se obremenitev pilotov in nosilnost pilota na konci v temeljih različno razprostirajo, saj na njih vplivata deformacija in rotacija plošče. Čeprav je bil najmanjši učinek na nasip opazen, ko je razpoka v tleh sekala nasip HŽ ortogonalno, tradicionalni modeli, ki to vključujejo, ne izpolnjujejo minimalnih varnostnih standardov. Rezultati te študije kažejo, da je posedek nasipa zaradi obremenitve z vlakom neznamen v primerjavi s posedkom zaradi razpoka v tleh. Zato je potrebno ta učinek prednostno upoštevati pri načrtovanju alternativnih nasipov HŽ, zlasti v območjih tal, kjer lahko nastanejo razpoke.

total and differential foundation settlement in regions where geological conditions are complicated, such as in areas where ground fissures are developed [3, 11, 19, 26]. At present, however, the design of GRPS embankments predominantly follows the engineering foundation design code [7, 17]. Studies that address their ability to cope with ground fissures and associated effects have rarely been reported in the literature.

In some mountainous areas, HSR routes inevitably intersect with ground fissures because of the terrain (Fig. 1). For example, 271 ground fissures have been mapped in the depressed Taiyuan Basin in Shanxi, China (Fig. 1). These tectonically controlled fissures are generally oriented parallel to the underlying fractures and are controlled by the regional stress field. Because these fractures are affected by the northwest-southeast tensile stress and the resultant sinistral shear couplet, they generally manifest as a series of northeast and north-northeast conjugate normal thrust faults (Fig. 1). The activities of these tectonically controlled fissures are known to be facilitated by the extraction of excess groundwater from the Taiyuan Basin [16]. As a result of our field investigation, 21 ground fissures developed in the Taiyuan Basin have been shown to pass through the Da-Xi HSR, which is currently under construction, at angles ranging from 15° to 90°; their interactions, combined with the extraction of excess groundwater, present significant risks to this ongoing project. Considering this problem, the Da-Xi HSR, built from Datong City of Shanxi Province to Xi'an City of Shaanxi Province with a total length of 859 km, has to reduce its maximum running speed to 250 km/h in the region of the Taiyuan Basin. In the basin, the railway line is designed generally along the strike direction of the flat area (Fig. 1). The lithology is relatively simple in the area. The main exposed layers of the Taiyuan Basin are Quaternary loess and silty clay

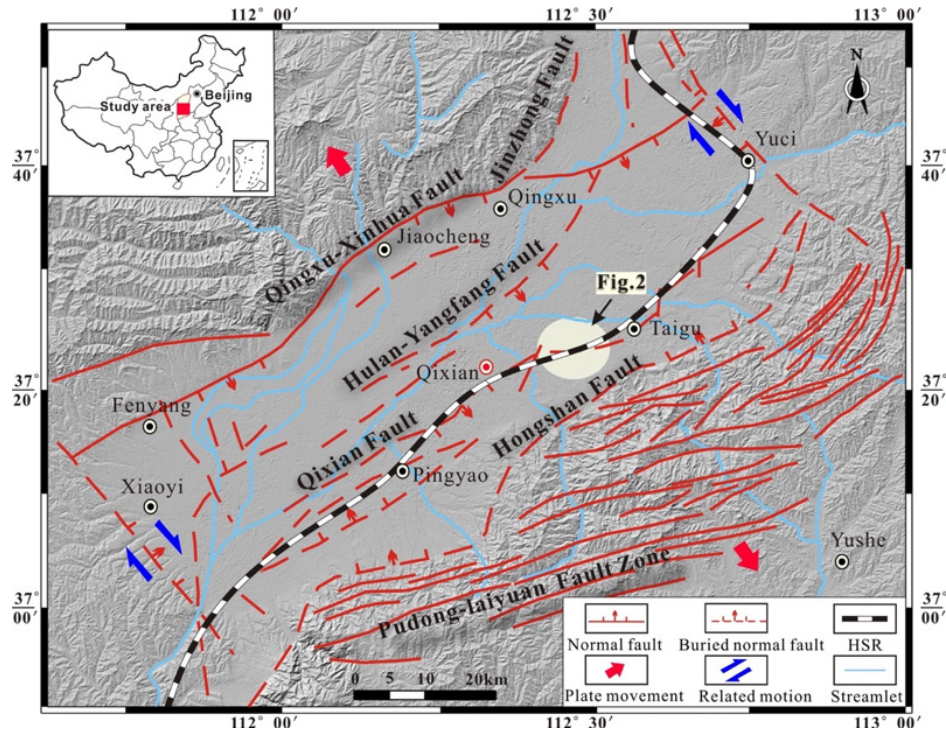


Figure 1. Regional tectonic map of the study area.

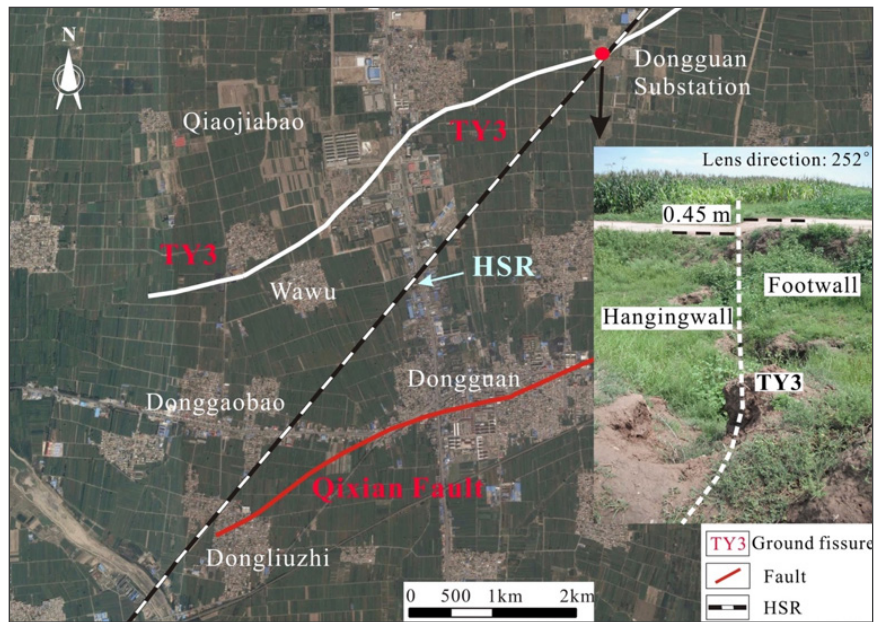


Figure 2. Map of the intersection angle between the TY3 fissure and the Da-Xi HSR.

with a thickness of approximately 50–80 m and 60–100 m, respectively, and the depth and thickness of the underground aquifer was investigated to be 50–80 m and 2–5 m, respectively.

Other than the relatively simple lithology under the HSR, the varied intersection angles between the fissures

and the HSR will likely result in a range of different kinds of damage. Ground fissures that intersect with the HSR at low angles create more significant engineering issues, as they will have a larger area of overlap. For example, because the TY3 ground fissure passes through the Da-Xi HSR at an angle of 15°, the overlap area is close to 80 m in length (Fig. 2). The offset of the TY3

fissure can be up to 0.45 m in areas close to the railway, and the average settling rate has recently been measured to be 4 mm per year [16]. Thus, the TY3 fissure should be prioritized in any studies on the influence of ground fissures on the Da-Xi HSR.

This study reports a series of reduced-scale experiments that were conducted to investigate the influence of ground fissures occurring at different intersection angles on the GRPS embankments of the Da-Xi HSR.

First, a reduced-scale test at an intersection angle of 15° (referred to as test #1) was conducted to simulate the embankment's response given at different TY3 ground-fissure offsets. Next, the effects of different intersection angles were investigated via additional reduced-scale tests at angles of 60° and 90°, respectively (referred to as tests #2 and #3, respectively). Finally, the ultimate cumulative settlement of the Da-Xi HSR subgrade induced by train loading was calculated and compared with the track settlement caused by ground fissures.

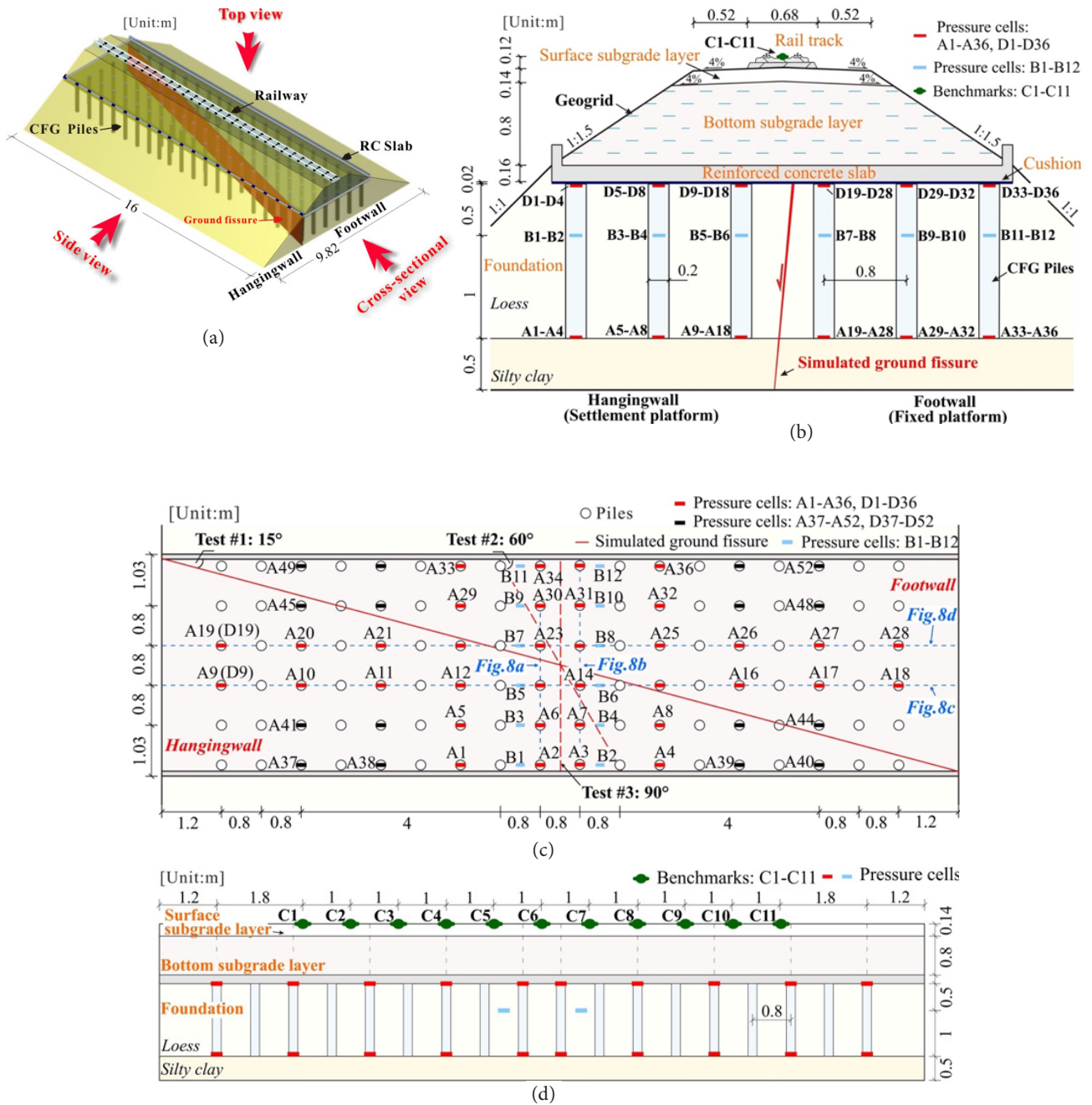


Figure 3. Setup of the reduced-scale physical model: (a) three-dimensional (3D) view; (b) cross-sectional view; (c) top view; (d) side view.

2 MATERIALS AND METHODS

2.1 Model construction

The TY3 ground fissure, which intersects with the Da-Xi HSR, was chosen as the case study, and a series of 1:5 scale embankment models were investigated (i.e., tests #1, #2, and #3). As part of the model-design process, geometric similarity $c_1 = 5$ with a primary variable was selected as the similarity criterion, while other physical quantities were derived using dimensional analyses. Thus, a model of the maximum dimensions was constructed, specifically a length of 16 m, a width of 9.82 m, and a height of 3.24 m (Fig. 3). The embankment models were designed strictly according to MRPRC guidelines [17], comprising a ballast-less rail track, subgrade, RC slab, and foundation (Fig. 3b).

In the models, the rail track is mainly comprised of a rail, an elastic fastener, double-block sleepers, a roadbed slab, and a support layer. The support layer is thus comprised a 0.03-m-thick layer of plain concrete with a strength class of C20, while a 0.05-m-thick RC layer with a concrete strength class of C40 was used to build the roadbed slab. The reinforced bars used in the roadbed slab were designed using the equal-strength principle, while the double-block sleepers were comprised of plain concrete blocks with a strength class of C40.

The subgrade layer was divided into two: graded gravel used to build the surface layer, while the lower layer was comprised of a mixture of coarse sand and graded gravel in the ratio 1:5.6. Several layers of polyester geogrid with a spacing of 0.12 m were also placed in the bottom subgrade layer (Fig. 3b). The particle size distribution in the graded gravel and coarse sand is shown in Fig. 4.

Loess and silty clay were used to remold the foundation, and the properties of the soil are summarized in Table 1. Note that the shear-strength parameters of the soil were determined using drained axial tests. A fine sand infill was used to simulate the ground fissures at a dip of 85°, as in the case study. Thus, the embankment passed obliquely through the ground fissure (Fig. 3b), while cement fly-ash gravel piles with a strength class of C15 were imbedded into the foundation (Fig. 3b and

3c). The pile length, diameter, and spacing were 1.5 m, 0.2 m, and 0.8 m, respectively, and a 0.02-m-thick plain concrete cushion formed the top layer. A 0.16-m-thick RC slab was cast on top of the plain concrete cushion to create a raft structure. The concrete used for both the cushion and the RC slab had a strength class of C30 and was manufactured from a mixture of cement, water, coarse sand, and gravel in the ratio 1:0.4:1.4:2.6. Two layers of rebar were also emplaced into the RC slab, again designed using the equal-strength principle.

2.2 Measurements

A number of cells were installed in the embankment model to measure the pressure on the two ends of the

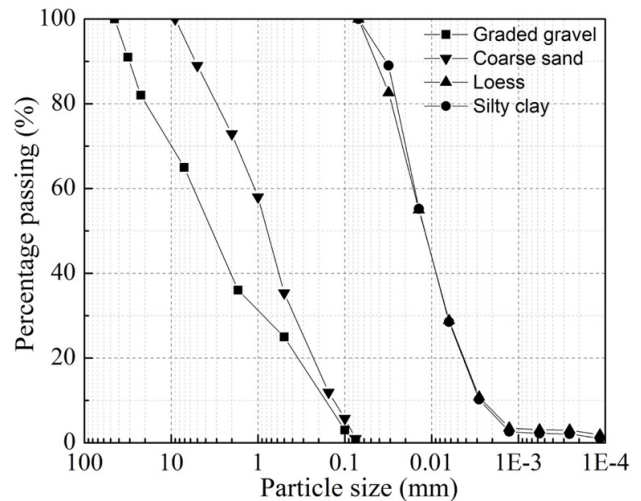


Figure 4. Particle size distribution of the materials used in the test.

Table 2. Reduced-scale model tests.

No.	Intersection angle (°)	Pile load (kPa)	Pile end-bearing (kPa)	Earth pressure (kPa)
#1	15°	D1-D36	A1-A36	B1-B12
#2	60°	D1-D52	A1-A52	B1-B12
#3	90°	D1-D52	A1-A52	B1-B12

Table 1. Properties of the soil used in the test.

Soil type	Specific gravity	Plastic limit (%)	Liquid limit (%)	Water content (%)	Unit weight (kN/m ³)	Cohesion (kPa)	Internal friction angle (°)
Loess	2.72	17.8	29.1	12	18	27	21
Silty clay	2.71	15.3	28.2	13.5	19.8	49	23

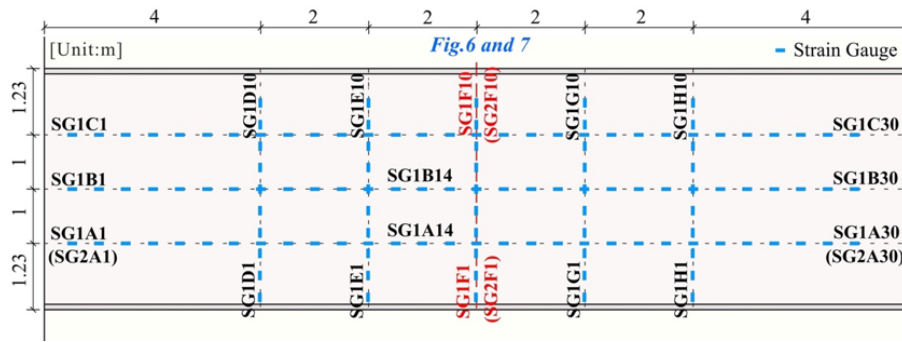


Figure 5. Layout of strain gauges used in the test.

piles (Fig. 3b-3d, Table 2). In tests #2 and #3, because the pressure cells D1-D52 installed on top of the piles were used to measure the pile load, 52 additional cells (A1-A52) were installed on the bottom of the piles to measure the end-bearing. In test #1, the lowest intersection angle, 36 pressure cells were installed on each end of the piles and were marked in red in Fig. 3c. In addition, 12 cells were installed in the loess layer to measure the foundation pressure, numbered B1-B12 (Fig. 3), while strain gauges were installed on both rebar layers to measure the deformation of the RC slab. The upper layer was numbered as the SG1 series, the lower layer was numbered as the SG2 series (Fig. 5), and the rail-track settlement was monitored in real time using precise levels from 11 benchmarks along the track (Fig. 3d).

2.3 Test implementation

The test procedure described here was implemented in the Foundation Settlement Simulation Laboratory at Chang'an University, China [20, 21]. To simulate the settlement of ground fissures in the hangingwall relative to the footwall, the side of the model with the settlement platform was set as the hangingwall, while the other side with a fixed platform was set as the footwall (Fig. 3b). Thus, the downward movement of the platform, which simulated the dislocation of the ground fissure, could be artificially controlled. In general, the measured average activity rate of the TY3 ground fissure has been about 4 mm per year. To predict the settling volumes of the ground fissures over the 50-year design service period of the HSR system, the offset in the test was set to 0.2 m, which is equivalent to the cumulative ground-

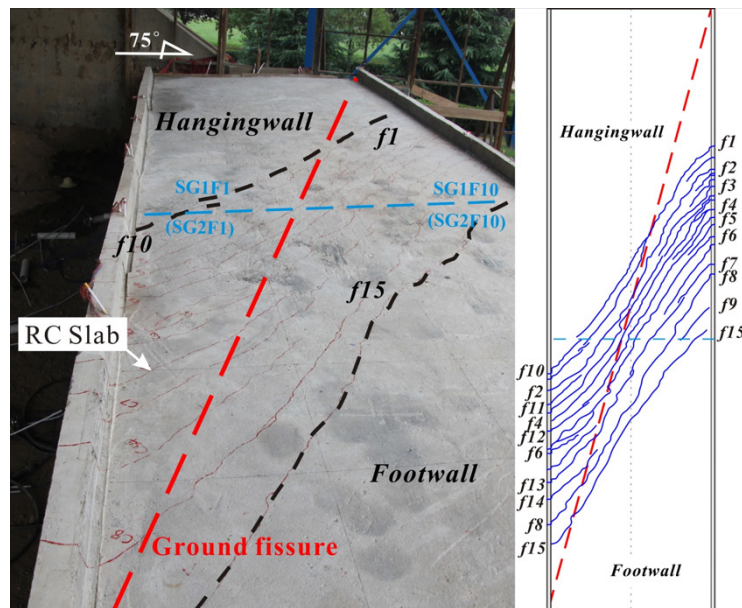


Figure 6. Photograph and diagram of cracks formed on the RC slab by the end of the experiment.

-fissure dislocation of 1.0 m in the case study. The test process was divided into 10 stages, each with a 0.02-m increment. At each stage, the model was stabilized for 24 h before the pressure, deformation, and settlement data were recorded.

3 TEST #1 OBSERVATIONS

3.1 Deformation of the RC slab

During test #1, as the settlement platform descended and the extent of the ground-fissure dislocation increased, such that the RC slab deformed a great deal, 15 cracks formed in the central area of the slab by the end of

the test (Fig. 6). The area where these cracks formed is subsequently referred to in this paper as the failure zone. As this zone is concentrated around the central area of the intersection of the RC slab and the ground fissure, this region was chosen for further deformational analysis. Variation in the rebar strain in the RC slab with respect to an increasing ground-fissure offset is presented in Fig. 7, wherein the two rebar layers showed significant differences in the strain variation with respect to the increasing ground-fissure dislocation. At a ground-fissure dislocation of 0.02 m, tensile strain was observed on the footwall side of the upper rebar layer and compressive strain was detected on the hangingwall side of this layer (Fig. 7a). At the same time, compressive strain was observed on each side of the lower rebar layer (Fig. 7b). In contrast, when the ground-fissure dislocation was larger than 0.02 m and was continuously increasing, areas on the hangingwall side of the upper rebar layer of rebar (e.g., SG1F4, SG1F5 and SG1F6) and the lower rebar layer (e.g., SG2F4 and SG2F5) transitioned to experience tensile rather than compressive strain (Fig. 7).

As described above, the dislocation at 0.02 m acted as a boundary for the variation of the rebar strain status on the hangingwall side. To further analyze the deformation of the RC slab, variations in the ground-fissure dislocation were divided into two phases by the dislocation at 0.02 m. In the first phase, as the dislocation increased to 0.02 m, compression was observed on the hangingwall side of the RC slab (see Fig. 7). At the same time, on the footwall side of the RC slab, tension was observed in the upper part of the slab, while compression occurred in the lower part, indicating that the footwall side was bending upwards to form a convex shape. In the second phase, when the dislocation was larger than 0.02 m, the hangingwall side of the RC slab experienced tension in both the upper and lower regions, which simultaneously increased with the dislocation of the ground fissure. The results also indicated that the footwall side of the RC slab continued to bend upwards as the dislocation of the ground fissure increased (Fig. 7). Indeed, the variation of the rebar strain presented in Fig. 7 can be explained by the relative movement between the hangingwall side and the footwall side of the RC slab. When the hangingwall side of the ground fissure descended slightly (e.g., a dislocation of 0.02 m in the model), the RC slab rotated to the hangingwall side accordingly, thus inducing a pressure to the hangingwall side by the self-weight of the footwall side and leading to an upward convex bend in the footwall side. Note that the rotation mechanism of the RC slab will be illustrated in detail later in Fig. 11. As the dislocation increased, the hangingwall side of the RC slab continued to descend with the ground fissure, pulling down its other side and leading to a tensile deformation in itself, and at the same time, aggravating the

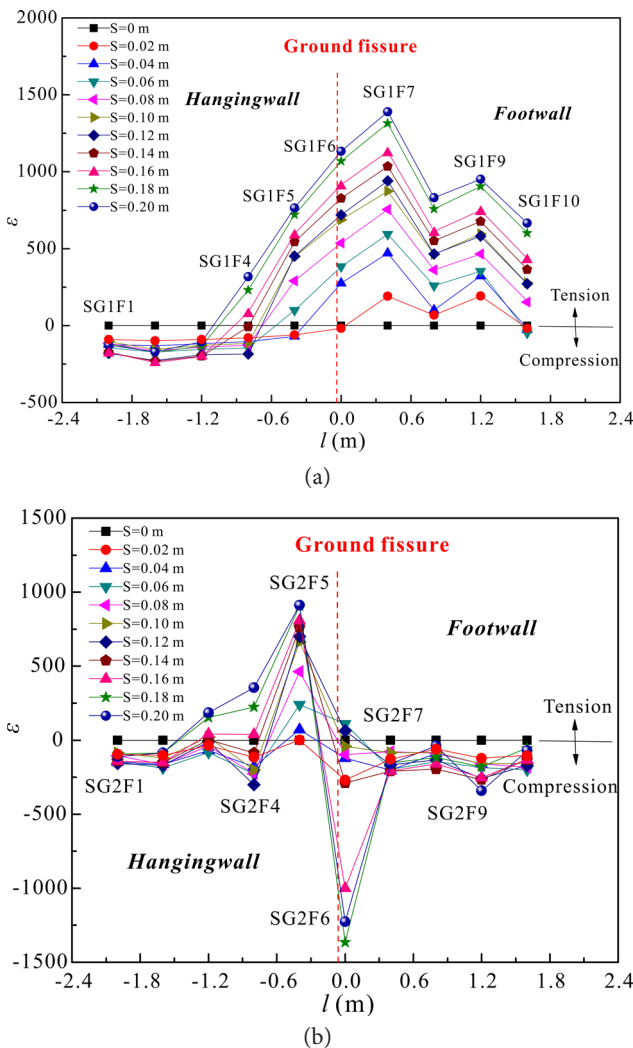


Figure 7. Variation in rebar strain in the RC slab with respect to the increasing dislocation of the ground fissure: (a) strain in the upper layer; (b) strain in the lower layer (Note *s*: dislocation of ground fissure; ϵ : rebar strain; *l*: position of the strain gauges in normal direction of the rail track)

upward convex bend in the footwall side. Thus, under the effect of the pull force created by the hangingwall side, both the tensile deformation on the hangingwall side and upward convex bending deformation on the footwall side increased dramatically in the RC slab near the ground fissure as the dislocation increased (Fig. 7). Finally, as a result of the ground-fissure dislocation, an integrated bend-tension failure of the RC slab was observed in the region near the ground fissure (Fig. 6 and 7).

3.2 Bearing piles in the foundation

As the settlement platform descended and the dislocation of the ground fissure increased, the end-bearing of the piles in the foundation also varied significantly. As observed in Fig. 8, the rate of change in each end-

-bearing was not constant with the increase in the dislocation of the ground fissure. The results indicated that variations in the end-bearing with increasing ground-fissure dislocations can be divided into two stages based on the rate of change: (i) the saltation stage, which refers to the dislocation of the ground fissure up to 0.02 m; and (ii) the development stage, which refers to the period of ground-fissure dislocation between 0.02 m and 0.2 m. During the saltation state, the end-bearings in the piles on the hangingwall side decreased rapidly, whereas those in the footwall all increased (Fig. 8). In contrast, during the development state, very small changes were observed in the pile end-bearings on the hangingwall side, whereas a good degree of variation was observed in those on the footwall side (Fig. 8). The results indicated that the pile

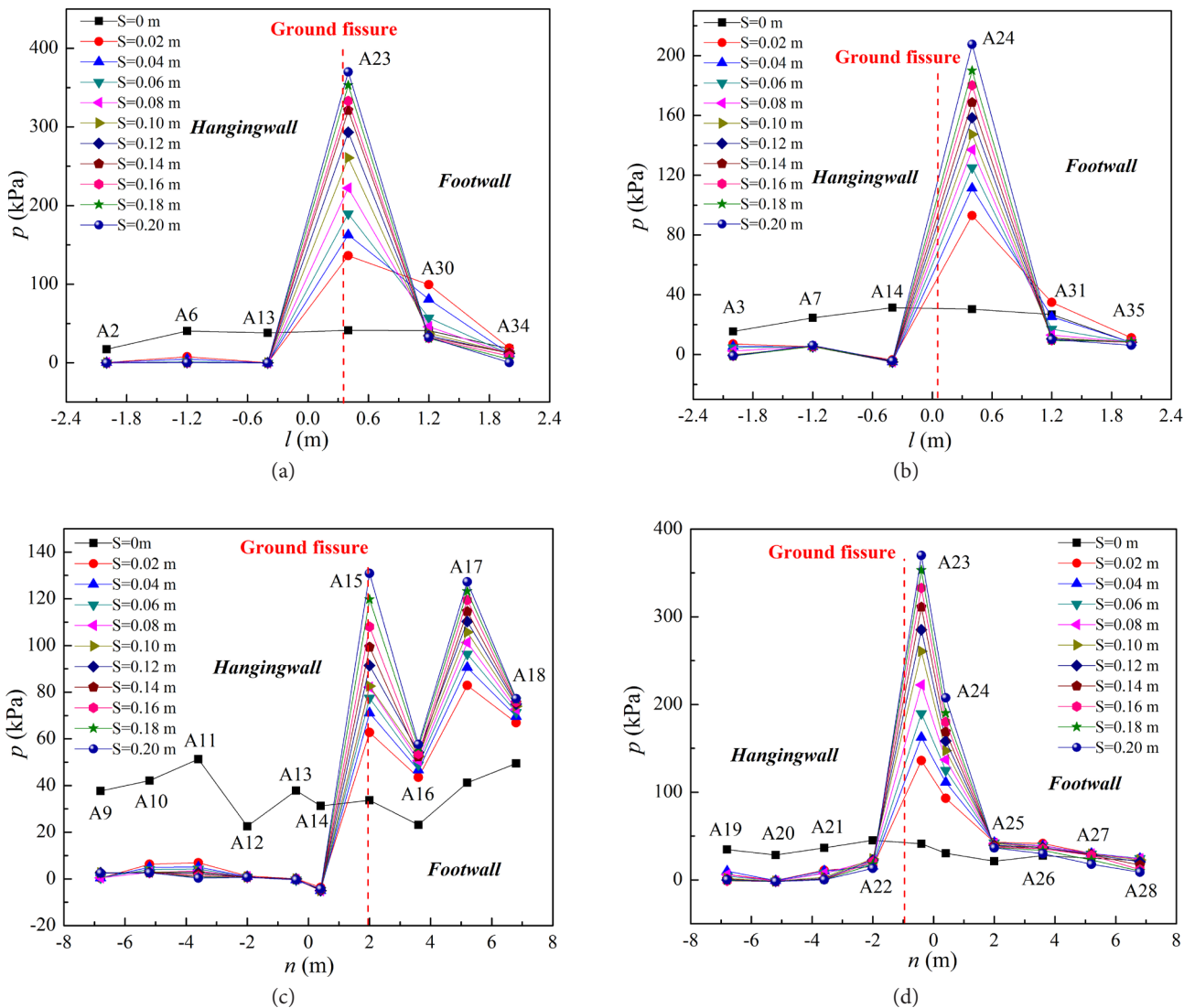


Figure 8. Variation in the end-bearing of piles with respect to the increasing ground-fissure dislocation (Note: s : ground-fissure dislocation; p : end-bearing of piles; l, n : position of the pressure cells in normal and tangential direction of rail track).

end-bearings closest to the ground fissure increased in concert with the dislocation (e.g., A23–A24 and A15–A16), whereas other end-bearings located further away from the fissure decreased with increasing dislocation (e.g., A30–A31 and A26–A28). These data indicate that variations in the end-bearings on the footwall side are correlated with the distance from the ground fissure.

Further analysis of all the end-bearings on the footwall side revealed a clear partition (Fig. 9); the end-bearings varied greatly during the development stage as the ground-fissure dislocation increased. Data from the end-bearings on the footwall side of the foundation can be divided into two zones according to the variations in the end-bearings. The test area that exhibited increased

pile end-bearings following enhanced ground-fissure dislocation is referred to as zone *i* (Fig. 9a), and zone *ii* denotes the area where the pile end-bearings first increased and then decreased with enhanced ground-fissure dislocation (Fig. 9(b)). In addition, the term ‘A-boundary’ is introduced to refer to the boundary regions between the two zones, *i* and *ii*. It should be noted that the A-boundary is used here to divide the footwall side of the foundation based on variations in the end-bearing given that the precise location of this boundary cannot be accurately determined. This is illustrated, for example, by the fact that variations in the end-bearings of A24 and A25 were different; the position of the A-boundary can only be determined in this case in these two piles, and the accurate location between the piles varied.

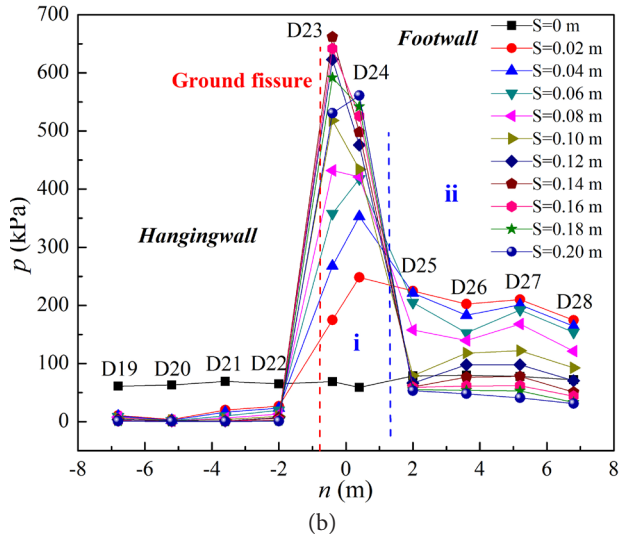
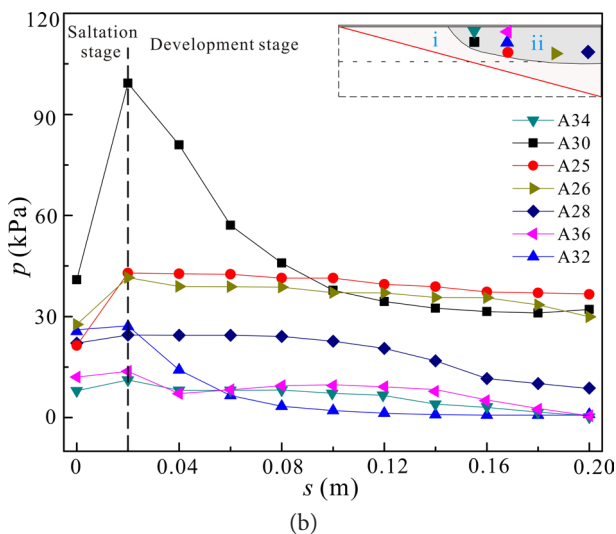
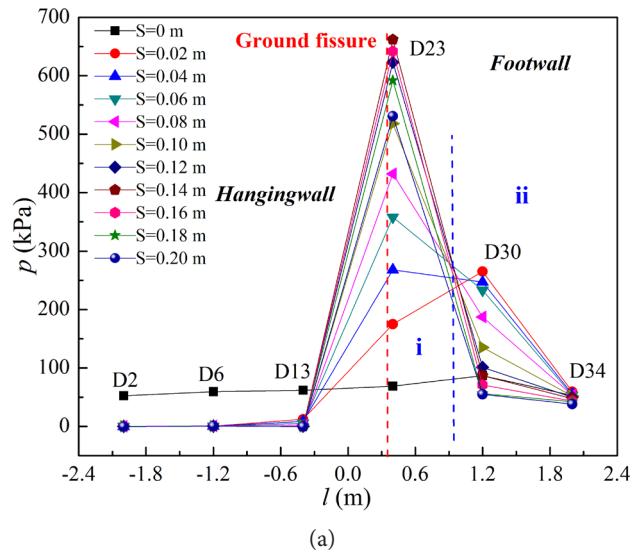
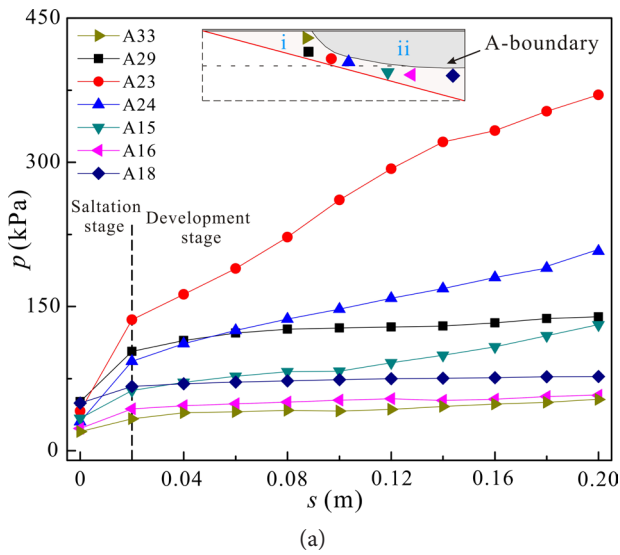


Figure 9. Variation in the end-bearing of the piles in footwall side with respect to the increasing ground-fissure dislocation: (a) zone *i*; (b) zone *ii* (Note: *s*: ground fissure dislocation; *p*: pile end-bearing).

Figure 10. Variation in pile loads with respect to the increasing dislocation of the ground fissure (Note: *s*: ground fissure dislocation; *p*: pile loads; *l*, *n*: position of the pressure cells in normal and tangential direction of rail track)

The results show that loads on the hangingwall side decreased by a large amount when the ground-fissure dislocation increased up to 0.02 m, similarly to the variation seen in the end-bearings (Fig. 10). As discussed above, a 0.02-m-thick plain concrete cushion was emplaced between the RC slab and the piles, which entirely encapsulated the tops of the piles and the bottom of the RC slab. Thus, the decrease in the pile loads and the end-bearings on the hangingwall side was inferred to have been induced by the relative movement between the soil and the piles in the foundations (Fig. 11). The results indicated that as the settlement platform descended and the amount of ground-fissure dislocation increased, the soil in the foundation also descended and the pile settlement was controlled by the deformation of the RC slab. In places where the soil settlement in the foundation exceeded the pile settlement, the end-bearings decreased. In contrast, both the end-bearings in the areas where the bottoms of the piles were out of contact with the surrounding soil (Fig. 11) decreased to zero (e.g., D2 and D6).

The data also indicated that the pile loads on the footwall side did not simply follow the division of the end-bearings. For example, the pile load D23 initially increased and then decreased as the ground-fissure dislocation increased; this pile was also divided into zone *i* due to variations in the end-bearing A23 (Figs. 8 and 10). Further analysis of all the pile loads classified into zone *i* increased as following enhancements in the dislocation, with the exception of D15 and D23, which increased initially before decreasing (Fig. 12a). The loads

for the piles in zone *ii* exhibited the same trend for the end-bearing variation, wherein an initial increase was followed by a reduction as the ground-fissure dislocation was enhanced (Fig. 12b; noted that just some typical values are shown in Fig. 12 due to space limitations).

A comparison of the pile load and the end-bearing from the same pile (Fig. 12) indicated that the former was much larger than the latter, indicating that the pile side friction bore the majority of the load. It can thus be concluded that the piles in the foundation are end-bearing friction piles (Fig. 11). Thus, a decrease in the load in zones *i* and *ii* can be induced by mobilizing the piles to the maximum bearing capacity or unloading the upper structure. The results indicated that in zone *i* the pile loads on D15 and D23 increased to a significantly high value before subsequently decreasing, while all the other pile loads continued to increase in concert with the ground-fissure dislocation. Therefore, it can be concluded that these piles reached their ultimate bearing capacity during the course of the experiment. In contrast, none of the pile loads in zone *ii* increased to a value as high as those for D15 and D23 before decreasing; it can be inferred that this decrease in the pile loads in zone *ii* was induced by the unloading of the upper structure.

As observed in the deformation of the RC slab, the footwall side bent upwards to form a convex shape as a result of the ground-fissure dislocation. The deformation of the RC slab may have induced a decrease in the pile load in the area where the slab bent upwards. However,

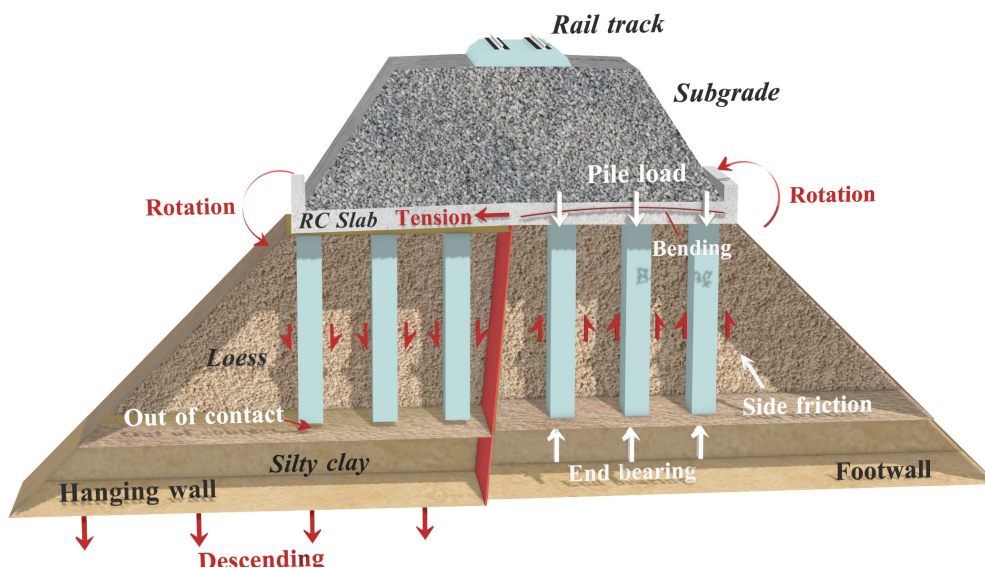


Figure 11. 3D illustration of bearing piles and mechanism of RC slab deformation.

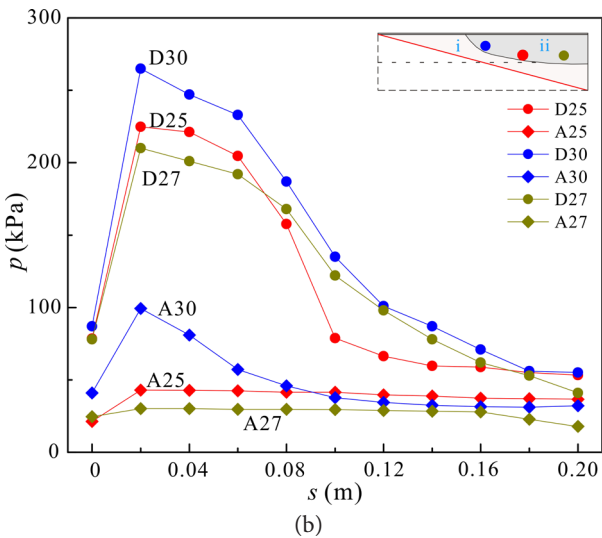
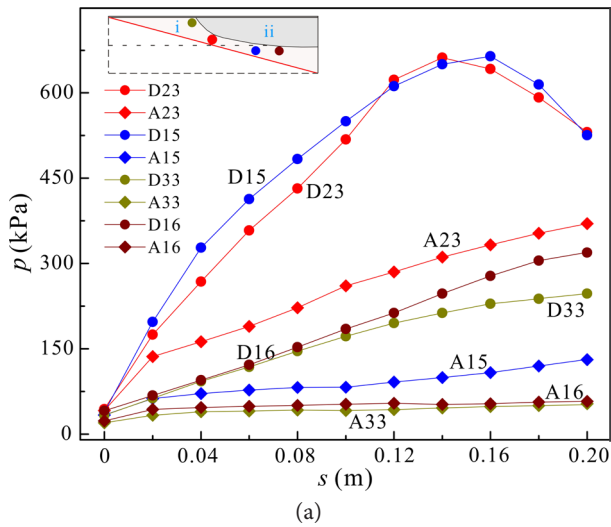


Figure 12. Comparison of pile load and pile end-bearing on the footwall side of the foundation: (a) zone i; (b) zone ii (Note: s is dislocation of ground fissure).

this shape change could not decrease the zone *ii* pile load while increasing the pile load in zone *i*. Thus, the variation in the pile loads indicates the RC slab was not just deformed because of the dislocation of the ground fissure, but was also rotated around this ground fissure (Fig. 11). The rotation of the RC slab induced load localization from the upper structure in zone *i* relatively closer to the ground fissure, while simultaneously unloading the upper structure in zone *ii*. Based on these results, the pile loads in zone *i* can continue to increase if it does not reach its ultimate bearing capacity. It should be noted that the rotation of the RC slab also induced the compression in the hanging side at a ground-fissure dislocation of 0.02 m.

The deformation and rotation of the RC slab was also reflected in the variations in the earth pressure in the

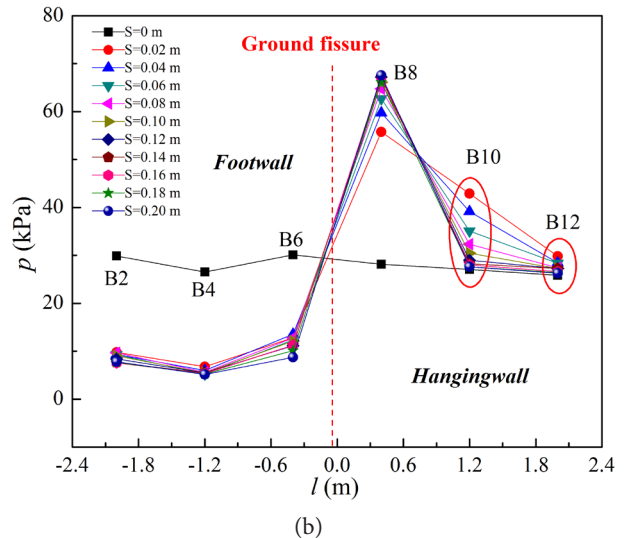
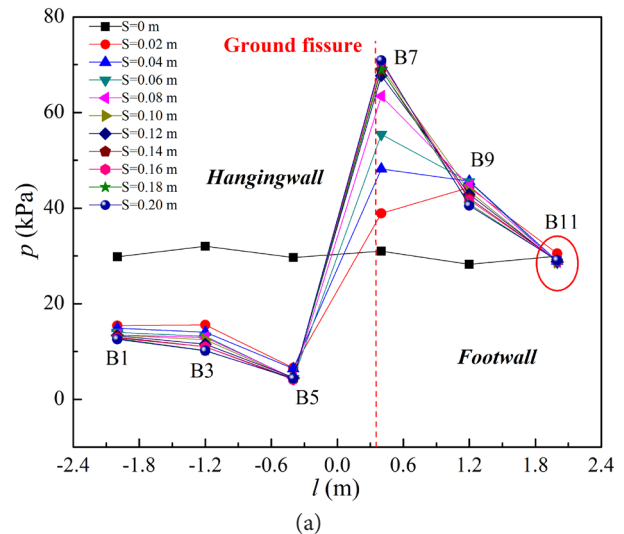


Figure 13. Variation in the earth pressure in the foundation with respect to the increasing dislocation of the ground fissure (Note: s : dislocation of ground fissure; p : earth pressure, l : position of the pressure cells in normal direction of rail track).

foundation (Fig. 13). The results show that the foundation pressure decreased on the hangingwall side as the dislocation of the ground fissure increased, whereas the foundation pressure on the footwall side area close to the ground fissure increased with the enhanced dislocation. The pressures measured in the areas relatively far from the ground fissure initially increased before decreasing as the dislocation enhanced (Fig. 13).

3.3 Rail-track settlement

The rail-track settlement in the model is illustrated in Fig. 14, wherein a positive value refers to settling and a negative value indicates lifting. The results indicate that the rail track on the hangingwall side underwent significant settling, whereas that on the footwall side was

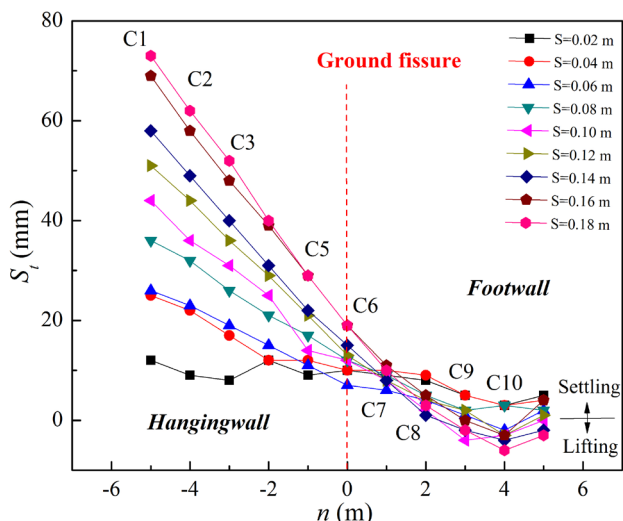


Figure 14. Variation in rail-track settlement as ground-fissure dislocation increased (Note: S_f : settlement of rail track; s : dislocation of ground fissure; n : position of the benchmarks in tangential direction of rail).

slightly raised (Fig. 14). Indeed, when the settlement platform descended by 0.02 m, the maximum rail-track settlement in the model reached 0.012 m. This indicates that a 0.1-m dislocation of the ground fissure in the case study can induce a maximum rail-track settlement of 0.06 m in the prototype scale. Based on the MRPRC guidelines [17], the post-settlement of the HSR should be less than 0.015 m. In other words, the 0.1-m dislocation of the ground fissure in the case study was already above the specified post-settlement limits. Given that the average measured activity rate of the TY3 ground fissure has recently been measured to be 4 mm per year [16], the presented data also indicates that the design of this embankment did not meet the 50-year service-period requirement at the point where it intersects the TY3 ground fissure.

4 EFFECT OF THE INTERSECTION ANGLES

4.1 Effect of the intersection angle on the RC slab deformation

Tests #2 and #3 were conducted to investigate the effects of the variable intersection angles that were run at 60° and 90°, respectively. The results indicated that the deformation and failure features of the RC slab on either side of the ground fissure in these tests were the same as in test #1. However, the failure zones, where the cracks formed on the RC slab when the settlement was 0.2 m, varied with the intersection angles (Fig. 15). The length of the failure zone was tangential to the rail track (i.e., the direction denoted by the axis x in Fig. 15) and decreased as the intersection angle increased. For example, the failure zone had lengths of $0.9W$, $0.49W$, and $0.31W$ for the intersection angles of 15°, 60°, and 90°, respectively, where W is the width of the RC slab. As presented in Fig. 15, the area of the failure zone on the footwall side, S_f and the area on the hangingwall side, S_h , also varied as the intersection angle increased. S_f is slightly larger than S_h , thereby indicating that the footwall side of the RC slab was more affected by the dislocation of the ground fissure. The results indicated that both the length and the area of the failure zone decreased in a non-linear fashion as the intersection angle increased (Fig. 15). The accuracy of this non-linear correlation could be further enhanced if more model tests incorporating different intersection angles were to be conducted. Indeed, varying trends in the length and area of the failure zone indicate that orthogonal intersections between the embankment and the ground fissure exhibited the least effect on the RC slab.

4.2 Effect of the intersection angle on the A-boundary

Rapid decreases in both the pile loads and the end-bearing of the piles on the hangingwall side were also

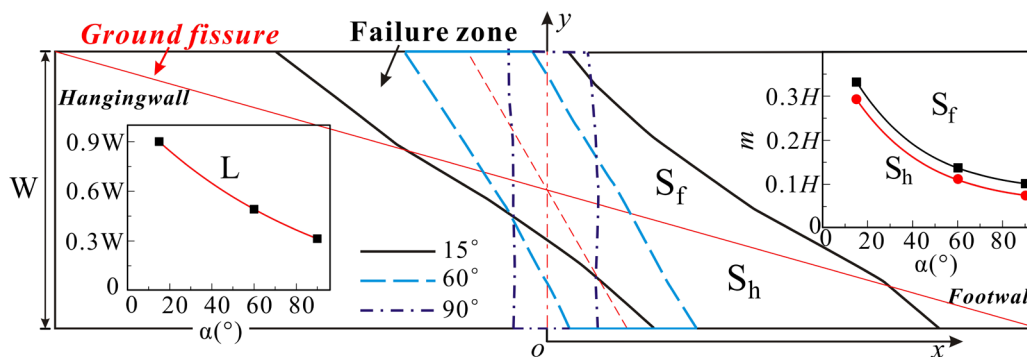


Figure 15. Analysis of the influence of the failure zone on the RC slab at different intersection angles (Note: S_f , S_h : area of the failure zone on the footwall and hanging wall side, respectively; m denotes the area of the failure zone at each side of the ground fissure; H : half area of the RC slab; α : intersection angle, L : length of failure zone in tangential direction of rail track).

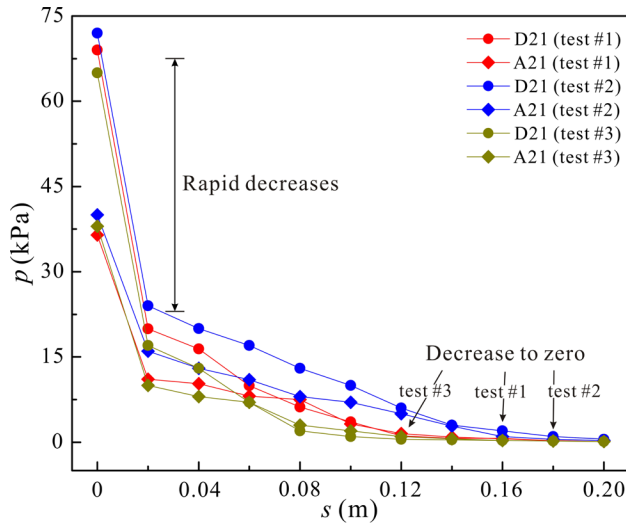
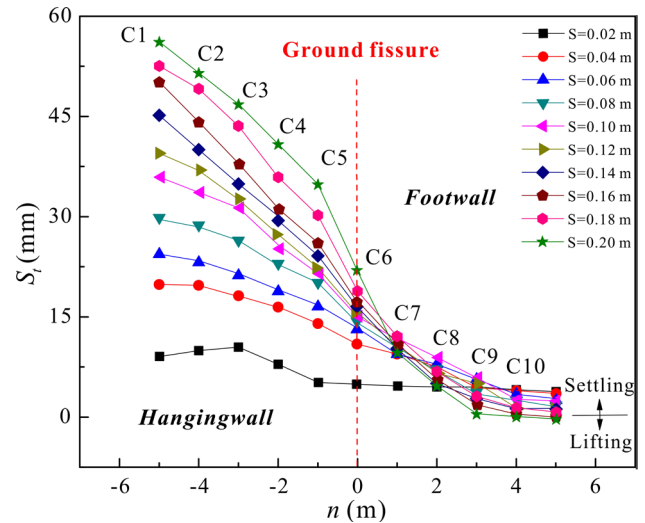


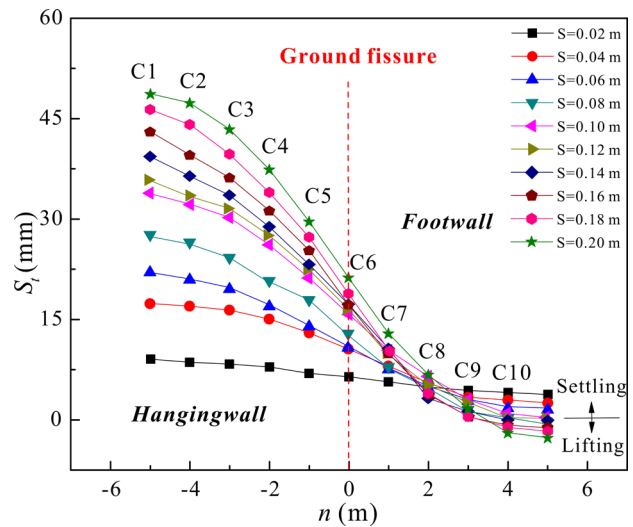
Figure 16. Rapid decreases in pile loads and end-bearing of piles on the hangingwall side.

detected in tests #2 and #3, as observed in D21 and A21 (Fig. 16). On the footwall side of the foundation, the results indicated that the A-boundary remained stable as the dislocation of the ground fissure increased, though this varied with the intersection angle (Fig. 17). The A-boundary remained approximately parallel to the ground fissure at different intersection angles, whereas the area of zone *i*, where the load of the upper structure was localized, decreased when the intersection angle increased. Indeed, at an intersection angle of 90°, zone *i* encompassed the smallest foundation area and exhibited the smallest number of piles mobilized to their ultimate bearing capacity (Fig. 17).

The results indicated that since the pile loads and the end-bearing exhibited differences in both characteristics and degrees of variation between zones *i* and *ii*, the A-boundary can be used to direct the foundation design of the embankment to intersect the ground fissures. For example, the number of piles in zone *ii* may be decreased, while simultaneously increasing the number in the zone to generate a more effective and economic design.



(a)



(b)

Figure 18. Analysis of the influence of different intersection angles on track settlement: (a) Test #2, (b) Test #3 (Note: S_i : settlement of rail track; s : dislocation of ground fissure; n : position of the benchmarks in tangential direction of rail).

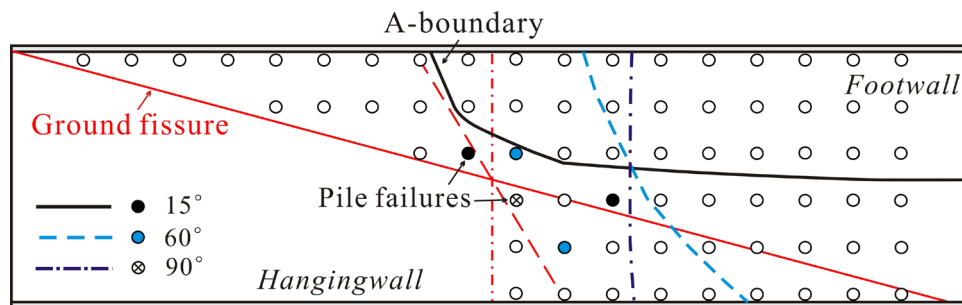


Figure 17. Analysis of the influence of different intersection angles on the position of the A-boundary.

4.3 Effect of the intersection angle on the rail-track settlement

The variations in the rail-track settlement as the ground-fissure dislocation increased (tests #2 and #3) are shown in Fig. 18. A comparison of the data presented in Figs. 18 and 14 indicates that, at the same ground-fissure dislocation, the maximum rail-track settlement decreased following an increase in the intersection angle. Indeed, in the case of the 0.02-m ground-fissure dislocation, the maximum rail-track settlements in tests #2 and #3 were 10.5 mm and 9 mm, respectively, which are 85% and 75% of that observed in test #1, respectively. Therefore, the results indicated that given one ground fissure with the same average activity rate, an HSR system with an orthogonally intersecting embankment will exhibit the longest service period. Taken in combination with the analysis of the effects of the intersection angle on the RC slab and foundations, embankments that intersect ground fissures orthogonally should be seriously considered when designing HSRs. Nevertheless, these results still do not prove that a GRPS embankment is suitable for the section of the Da-Xi HSR that intersects the TY3 ground fissure. As shown in test #3, a 0.02-m ground-fissure dislocation can induce a maximum settlement of 9 mm in the model track, which is equivalent to a 45-mm track settlement in the actual embankment and is above the limit specified by MRPRC [17]. Thus, to meet the required 50-year design service period for a HSR system, further research is necessary to develop a suitable embankment design that can cope with the bend-tension deformation of the RC slab and further decrease the rail-track settlement. In addition, it is suggested that the A-boundary was used as the reference to arrange the piles in the foundation.

5 RAIL-TRACK SETTLEMENT INDUCED BY TRAIN LOADING

During the operation of the Da-Xi HSR, the post-settlement of the rail track included a combination of ground-fissure dislocation-induced and train-loading post-settlement. Thus, the present study analyzed the train-loading-induced settlement to generate comparisons with the settlement induced by the ground fissures. Because the effects of the geogrid were ignored to simplify the presented calculation, the estimates for the train-loading-induced settlement were amplified and will be larger than the values observed in reality. The train-loading-induced settlement was estimated using a layer-wise summation method and was assumed to be equivalent to the strip load on the subgrade surface, as specified by German Railway Standards [7], due to

the high stiffness of the ballast-less rail-track structure. Thus, the dynamic stress induced by train loading in the subgrade with respect to the depth can be calculated as follows:

$$\sigma_z = \frac{2p_0}{\pi} \left(\frac{n}{1+n^2} + \tan^{-1} \frac{1}{n} \right) \quad (1)$$

where p_0 is the dynamic stress on the subgrade surface; z is the depth from the subgrade surface; and $n = z/b$, where b is the half width of the stress distribution on the subgrade surface.

However, since no field data for p_0 can be measured from the Da-Xi HSR, data from German Railway Standards [7] was used to estimate the dynamic stress in the subgrade. Applying p_0 to equation (1), the dynamic stress distribution along the depth of the subgrade in the Da-Xi HSR was obtained (Fig. 18). The results indicated a dynamic stress at the subgrade base of less than 2 kPa at a subgrade thickness in the actual embankment of 4.7 m (Fig. 18). In other words, the train loading insignificantly influenced the foundation settlement. The results of this study show that the cumulative settlement caused by the train loading was mainly limited to the subgrade zone. Thus, if this 4.7-m-thick subgrade layer was divided into 14 layers with thicknesses of 0.35 m, according to Chen et al. [4], the ultimate accumulative settlement of the Da-Xi HSR subgrade can be calculated by the layer-wise summation method as follows:

$$S_\infty = \sum_{i=1}^n \varepsilon_0^p \left(\frac{Li}{100} \right)^k \frac{p_{ref} + p_m}{s + m(p_{ref} + p_m) - (q_{ref} + q_m)} \quad (2)$$

where n is the number of layers and i ranges from 1 to 14; $L = \sqrt{p_{ref}^2 + q_{ref}^2}$, where p_{ref} and q_{ref} refer to the peak

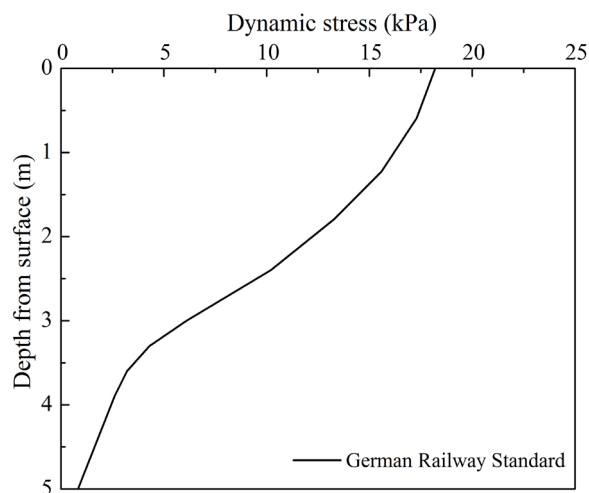


Figure 19. Graph showing the dynamic stress distribution as a function of depth.

mean stress and the peak deviatoric stress caused by the cyclic train loading, respectively; p_m and q_m are the initial mean stress and the initial deviatoric stress caused by the self-weight of the HSR subgrade, respectively; the material parameters ε_0^p and k can be determined using dynamic load tri-axial tests; and s and m are related to the strength parameters c and φ , respectively, which can be calculated as follows:

$$m = \frac{6 \sin \varphi}{3 - \sin \varphi}, \quad S = \frac{6 \cdot \cos \varphi}{3 - \cos \varphi} \quad (3)$$

In the reduced-scale model, the water content of the surface and bottom layers of the subgrade were 4.5% and 5.8%, respectively. Thus, the tri-axial and dynamic load tri-axial tests were performed on the materials in these two subgrade layers with corresponding water contents. In the tri-axial tests, the apparent cohesion, c , and the internal friction angle, φ , were measured at 0 kPa and 42°, respectively, for the graded gravel in the surface subgrade layer, and 0 kPa and 46°, respectively, for the coarse sand and graded gravel mixture in the bottom layer of the subgrade. The material parameters ε_0^p and k were measured using dynamic load tests at 0.0019 and 0.318, respectively, for the surface subgrade layer, and 0.0015 and 0.357, respectively, for the bottom subgrade layer. Thus, incorporating these parameters into equations (2) and (3), the ultimate accumulative settlement of the Da-Xi HSR subgrade was calculated to be 3.7 mm. However, as noted above, even if this train-loading-induced settlement was magnified, it was still relatively small compared to that induced by the ground-fissure dislocation in the case study. Priority must, therefore, be given to the study of the embankment design to cope with the ground fissures.

6 CONCLUSIONS

The present study conducted and reported a series of reduced-scale experiments to investigate the influence of ground fissures on HSR embankments at different intersection angles. A sensitivity analysis was used to investigate the effects of the intersection angles on the RC slab deformation, the stress state of the bearing piles, and the track settlement. The train-load-induced settlement of the embankment was then estimated using the analytical model put forward by Chen et al. [4] and then compared with the settlement induced by the ground-fissure dislocation. Five conclusions can be drawn based on this research.

1. The deformation of the RC slab can be divided into two phases due to the differences in the strain features on the hangingwall side with respect to increases

in the dislocation of the ground fissure. The strain data indicates that the RC slab underwent integrated bend-tension failure as a result of the action of the ground fissures, whereas the deformation phase and failure mode of the slab were independent of the intersection angle.

2. The pile load and the end-bearing of the piles on the hangingwall side of the foundations decreased rapidly when the dislocation of the ground fissure increased from zero to 0.02 m. Thus, the footwall side of the foundation can be divided into zones i and ii based on the variations in the pile loads and the end-bearings. A reduction in the pile loads of zone i was induced by the failure of the mobilized piles due to their ultimate bearing capacity, whereas the decrease in the pile loads and the end-bearings observed in zone ii was induced by the unloading of the upper structure associated with the deformation and rotation of the RC slab.
3. The analysis of the effect of the intersection angle quantitatively explained the minimal effect exerted by a ground fissure orthogonally intersecting on the embankment. The results indicated that the length and area of the failure zone of the RC slab decreased non-linearly following an increase in the intersection angle. In addition, the boundary between zones i and ii , termed the A-boundary, was dependent on the intersection angle and was independent of the ground-fissure dislocation.
4. As a result of the effect of the intersection angle on the track settlement, the GRPS embankment was deemed unsuitable for use in this specific Da-Xi HSR section. However, further research is required to propose an appropriate embankment design solution to cope with the bend-tension deformation in the RC slab. The A-boundary was suggested as a reference to arrange the foundation piles, thereby generating a more effective and economic overall design.
5. The ultimate cumulative settlement of the subgrade in the Da-Xi HSR was estimated to be 3.7 mm. The settlement induced by the train load was extremely small as compared to that induced by the ground fissure, and is a variable that should be considered when designing the HSR.

Acknowledgments

This research was funded by the grants from the Major Program of National Natural Science Foundation of China (Grant No. 41790441), the National Key Research and Development Program of China (Grant Nos. 2017YFC1502506, 2017YFC0505304, 2017YFC050530302, 2018YFC1505201), the Opening Fund of State Key Laboratory of Geohazard Prevention

and Geoenvironment Protection, Chengdu University of Technology (Grant No. SKLGP2019K001), the Special Fund for Basic Scientific Research of Central Colleges, Chang'an University (Grant No. 300102269506), the National Natural Science Foundation of China (Grant No. 41807234, 41302252).

REFERENCES

- [1] Augustin, S., Gudehus, G., Huber, G., Schüemann, A. 2003. Numerical model and laboratory tests on settlement of ballast track, in: Popp, K., Schiehlen, W. (Eds.), *System dynamics and long-term behavior of railway vehicles, track and subgrade*. Springer Verlag, Berlin, pp. 317-336.
- [2] Bell, J.W., Price, J.G., Mifflin, M.D. 1992. Subsidence-induced fissuring along preexisting faults in Las Vegas Valley, Nevada. *Proc. 35th Annual Meeting of the Association of Engineering Geologists*, Los Angeles, pp. 66-75.
- [3] Calçada, R., Delgado, R., Matos, A.C.E. 2009. *Bridges for High-Speed railways*. Taylor & Francis Group, London.
- [4] Chen, R., Jiang, P., Ye, X., Bian, X. 2016. Probabilistic analytical model for settlement risk assessment of High-Speed Railway subgrade. *J. Perform. Constr. Facil.* 30, 3. doi: 10.1061/(ASCE)CF.1943-5509.0000789
- [5] Dethy, B., Bouhenni, S. 2004. High Speed Lines in Belgium: Various engineering geological and geotechnical aspects. *Engineering Geology for Infrastructure Planning in Europe* 104, 485-503. doi: 10.1007/978-3-540-39918-6_55
- [6] Filippis, L.D., Anzalone, E., Billi, A., Faccenna, C., Poncia, P.P., Sella, P. 2013. The origin and growth of a recently-active fissure ridge travertine over a seismic fault, Tivoli, Italy. *Geomorphology* 195, 2, 13-26. <https://doi.org/10.1016/j.geomorph.2013.04.019>
- [7] German Railway Standard, 2008. *Erdbauwerke planen, bauen und in-stand halten [Earthworks plan, build and maintain]*. Ril 836, Berlin (in German).
- [8] Holzer, T.L., Davis, S.N., Lofgren, B.E. 1979. Faulting caused by groundwater extraction in southcentral Arizona. *Journal of Geological Research* 84, 82, 603-612. doi: 10.1029/JB084iB02p00603
- [9] Holzer, T.L. 1984. Ground failure induced by groundwater withdrawal from unconsolidated sediment. *Reviews in Engineering Geology* 6, 67-106. doi: 10.1130/REG6-p67
- [10] Huang, R.Q., Li, Y.R., Qu, K., Wang, K. 2013. Engineering geological assessment for route selection of railway line in geologically active area: a case study in China. *J. Mt. Sci.* 10, 4, 495-508. doi: 10.1007/s11629-013-2660-2
- [11] Jiang, Y., Han, J., Zheng, G. 2014. Numerical analysis of a pile-slab-supported railway embankment. *Acta Geotechnica* 9, 499-511. doi: 10.1007/s11440-013-0285-9
- [12] Kreitler, C.W. 1977. *Fault Control of Subsidence*, Houston, Texas. *Ground Water* 15, 3, 203-214. doi: 10.1111/j.1745-6584.1977.tb03165.x
- [13] Lee, C., Zhang, J., Zhang, Y. 1996. Evolution and origin of the ground fissures in Xian, China. *Engineering Geology* 43, 1, 45-55. doi: 10.1016/0013-7952(95)00088-7
- [14] Leonard, R.J. 1929. An earth fissure in southern Arizona. *Journal of Geology* 37, 8, 765-774.
- [15] Lofgren, B.E. 1978. Hydraulic stresses cause ground movement and fissures, Picacho, Arizona. *Geological Society of America Abstracts with Programs* 10, 3, 113.
- [16] Meng, L.C. 2011. *Study on the Formation Mechanism of Ground Fissures in Shanxi Fault Basin*. Dissertation, Chang'an University (in Chinese).
- [17] Ministry of Railways of the People's Republic of China (MRPRC), 2009. *Design code for High Speed Railway*. TB10621-2009, China Railway Press, Beijing.
- [18] Narasimhan, T.N. 1979. The significance of the storage parameter in saturated-unsaturated groundwater flow. *Water Resources Research* 15, 3, 569-576. doi: 10.1029/WR015i003p00569
- [19] Nordic Geotechnical Society, 2002. *Nordic handbook. Reinforced soils and fills*. Nordic Geotechnical Society, Stockholm.
- [20] Peng, J.B., Chen, L.W., Huang, Q.B., Men, Y.M., Fan, W., Yan, J.K. 2013. Physical simulation of ground fissures triggered by underground fault activity. *Engineering Geology* 155, 14, 19-30. doi: 10.1016/j.enggeo.2013.01.001
- [21] Peng, J.B., He, K., Tong, X., Huang, Q.B., Liu, C. 2016. Failure mechanism of an underground metro tunnel intersecting steep ground fissure at low angle. *Int. J. Geomech.* 17, 5, doi: 10.1061/(ASCE)GM.1943-5622.0000677
- [22] Pratt, W.E., Johnson, D.W. 1926. Local subsidence of the Goose Creek oil field. *Journal of Geology* 34, 7, 557-590.
- [23] Sarkar, I. 2004. The role of the 1999 Chamoli earthquake in the formation of ground cracks. *J. Asian Earth Sci.* 22, 5, 529-538. doi: 10.1016/S1367-9120(03)00093-2
- [24] Shaer, A.A.I., Duhamei, D., Sab, K., Foret, G., Schmitt, L. 2008. Experimental settlement and dynamic behavior of a portion of ballasted railway

- track under high speed trains. *Journal of Sound and Vibration* 316, 1, 211-233. doi: 10.1016/j.jsv.2008.02.055
- [25] Sun, Q., Indraratna, B., Nimbalkar, S. 2016. Deformation and degradation mechanisms of railway ballast under high frequency cyclic loading. *J. Geotech. Geoenviron. Eng.* 142, 1. doi: 10.1061/(ASCE)GT.1943-5606.0001375
- [26] Wang, J., Wang, J., Liu, J., Li, C., Yang, R. 2000. *Theory of ground fissures hazards and its application*. Shanxi Science and Technique Publishing House, Xi'an (in Chinese with English abstract).
- [27] Wang, Z.F., Shen, S.L., Cheng, W.C., Xu, Y.S. 2016. Ground fissures in Xi'an and measures to prevent damage to the Metro tunnel system due to geohazards. *Environ. Earth Sci.* 75, 6, 511-522. doi: 10.1007/s12665-015-5169-x
- [28] Xu, L.Q., Li, S.Z., Cao, X.Z., Somerville, I.D., Suo, Y.H., Liu, X., Dai, L.M., Zhao, S.J., Guo, L.L., Wang, P.C., Cao, H.H. 2016. Holocene intracontinental deformation of the northern North China Plain: Evidence of tectonic ground fissures. *Journal of Asian Earth Sciences* 119, 1, 49-64. doi: 10.1016/j.jseaes.2016.01.003
- [29] Zhang, Y., Wang, Z.C., Xue, Y.Q., Wu, J.C., Yu, J. 2016. Mechanisms for earth fissure formation due to groundwater extraction in the Su-Xi-Chang area, China. *Bull. Eng. Geol. Environ.* 75, 2, 745-760. doi: 10.1007/s10064-015-0775-0